Multifrequency transcranial ultrasound holography with acoustic lenses

Maxime Daniel, David Attali, Thomas Tiennot, Mickael Tanter, Jean-François Aubry

To cite this version:

Maxime Daniel, David Attali, Thomas Tiennot, Mickael Tanter, Jean-François Aubry. Multifrequency transcranial ultrasound holography with acoustic lenses. Physical Review Applied, 2024, 21 (1), pp.014011. 10.1103/PhysRevApplied.21.014011 . hal-04485338

HAL Id: hal-04485338
https://hal.science/hal-04485338v1

Submitted on 1 Mar 2024

Multi-frequency transcranial ultrasound holography with acoustic lenses

M. Daniel[1], D. Attali[1,2], T. Tiennot[1], M. Tanter[1] and JF. Aubry[1*]

[1]Physics for Medicine Paris, Inserm U1273, ESPCI Paris, PSL University, CNRS UMR 8063, 75015 Paris, France
[2]GHU-Paris Psychiatrie et Neurosciences, Hôpital Sainte Anne, Université Paris Cité, 75014 Paris, France

Focusing ultrasound through the skull requires accurate correction of skull induced aberrations. Acoustic lenses provide an inexpensive and effective measure for correcting these distortions. This study explores a phase unwrapping technique for designing multi-frequency acoustic lenses coupled with geometrically focused transducers. Here, we demonstrate numerically and theoretically that in a homogeneous medium and for a single target steered from the natural focus of the transducer, a wrapped lens can only work at its design frequency, while a phase unwrapped lens is broadband. This concept is further explored in experiments where three human skulls are inserted between a transducer and its natural focus. Unwrapped lenses are used to correct for the skull aberrating effect at multiple frequencies and are compared to their wrapped counterparts. Such experiments demonstrate that the unwrapped lenses are the only ones capable of correcting for skull aberrations in a broad range of frequencies. At the design frequency of the lenses, the unwrapped lenses perform quantitatively better than their wrapped counterparts since the average intensity behind three skulls was found to be 49% lower with a phase wrapped lens compared to a phase unwrapped lens, even if both allow to qualitatively refocus the wave at the desired targets. In addition, such results confirm the necessity to correct for skull aberrations, since the field may be highly distorted in the absence of aberration correction.

I. INTRODUCTION

Focused ultrasound is an emerging and promising technology which has been successfully used to treat patients with a variety of indications [1–3]. Targeting the brain with ultrasound has long been hampered by the defocusing effect of the skull bone [4]. Nevertheless, focusing waves in complex media has been a major subject of interest in various fields of research. In optics, several techniques have been proposed and are based on wave front shaping [5], measuring the transmission matrix of the scattering medium [6], phase conjugation [7], time-reversed ultrasonically encoded optical focusing [8] or machine learning approaches [9]. Aberrations correction methods have been implemented specifically for ultrasound transcranial focusing, such as time reversal [10] or phase conjugation [11]. Nevertheless, these techniques require the use of multi-element transducers and led to an ever-increasing number of transducer elements to improve the compensation of skull aberrations: from 64 in 2000 [11] to 300 in 2003 [12] and 1372 in 2010 [13]. Using a large number of transducers imposes severe constraints on the power electronics.

Varying-thickness acoustic lenses have thus been introduced to induce phase shifts on the wave front emitted by a single-element transducer [14–16] with a limited cost and for a given frequency [17–25]. Thin lenses, based on the wrapping of the phase were first developed in the context of MR-guided non-invasive surgery, where a flat transducer was coupled with a thin lens to allow the wave to be focused at the intended target, while minimizing the size of the whole ultrasound setup and freeing space in the MR bore [26].

When it comes to achieving a multi-frequency aberration correction, optics paved the way with the work conducted on chromatic aberrations correction [27–29]. In medical ultrasound, such multi-frequency aberration correction could be useful in the field of non-invasive neurostimulation [30], in order to find the optimal frequency to stimulate a given brain area [31,32] and for broadband transcranial therapies like brain histotripsy [33].

The aim of this work is to present the impact of phase unwrapping on acoustic lenses coupled with a geometrically focused transducer. First, numerical simulations are performed in a homogeneous medium while targeting a point laterally steered from the geometric focus of the transducer. The unwrapped and wrapped lens profiles are computed at a given frequency and the propagation of the wave through the lenses is performed at multiple frequencies to show the impact of phase unwrapping. Then, an application of phase unwrapping is shown on transcranial experiments performed at multiple frequencies with a single acoustic lens.

II. METHODS

A. Numerical simulations in a homogeneous medium

A proof of concept numerical experiment was first performed in a homogeneous medium with a 100 mm aperture and 100 mm radius of curvature spherical transducer. Its aim was to design an acoustic lens able to

---

[*] jean-francois.aubry@espci.fr

focus the wave at four different frequencies ($\nu_S = 250$ kHz, 500 kHz, 750 kHz and 1000 kHz) on a target steered laterally from the natural focus of the transducer by 0.75 cm. All lenses were designed using the frequency $\nu_D = 500$ kHz.

Simulations were performed by solving the wave equation using pseudo-spectral methods. Such methods are implemented in the k-Wave MATLAB toolbox [34], which, for a lossless heterogeneous medium, solves the following set of equations [35]:

$$\begin{cases} \dfrac{\partial \mathbf{u}}{\partial t} = -\dfrac{1}{\rho_0}\nabla\rho & \text{(momentum conservation)} \\ \dfrac{\partial \rho}{\partial t} = -\rho_0 \nabla\cdot\mathbf{u} - \mathbf{u}\cdot\nabla\rho_0 & \text{(mass conservation)} \\ p = c_0^2(\rho + \mathbf{d}\cdot\rho_0) & \text{(pressure} - \text{density relation)} \end{cases}$$

where $\mathbf{u}$ is the particle velocity, ρ the acoustic density, ρ_0 the equilibrium density, $\mathbf{d}$ the particle displacement, c_0 the isentropic sound speed and p the acoustic pressure.

If the medium is homogeneous, the terms $-\mathbf{u}\cdot\nabla\rho_0$ in the mass conservation equation and $c_0^2\mathbf{d}\cdot\rho_0$ in the pressure-density relation vanish. All simulations were performed with a spatial step $\Delta x = \Delta y = \Delta z = 248\ \mu$m which corresponds to 6 points per wavelength in water at the highest frequency (1 MHz).

The algorithm developed to determine the lens profile can be described as follows:

1. A virtual source of unit amplitude (corresponding to the target) is placed in the focal plane of the transducer, but laterally steered from the geometric focus.
2. A set of virtual sensors are distributed at the surface of the transducer to record the simulated field emitted by the source at a design frequency ν_D. The phase on each sensor is computed by performing a Fourier transform on a 5-period window once the steady state of the pressure signal has been reached, yielding a wrapped phase map, constrained to $[-\pi, \pi]$.
3. The phase map is transformed in a thickness map using the formula:
$$e(M) = \frac{\Phi(M)}{2\pi\nu_D}\frac{1}{\dfrac{1}{c_{\text{water}}} - \dfrac{1}{c_{\text{lens}}}} + K, \qquad \text{(II.1)}$$
where $\Phi(M)$ is the phase map, c_{water} the sound speed in water (equal to 1485 m/s), c_{lens} the sound speed in the acoustic lens material (equal to 1000 m/s) and K is a constant thickness of 2 mm added for structural stability purposes.

A second lens profile was investigated. The algorithm was the same except that the wrapped phase map was post-processed in order to obtain an unwrapped phase map, which is not constrained in the interval $[-\pi, \pi]$. Several unwrapping algorithms have been developed, based for instance on branch cuts [36] or network flow [37]. We used the unwrapping algorithm based on the transport of the intensity equation, introduced by Zhao and colleagues [38].

B. Skull imaging and acoustic modelling

Transcranial experiments were performed on three skulls (referenced as A, B and C), which were provided by the Institute of Anatomy (UFR Biomédicale des Saints-Pères, Université Paris Descartes, Paris, France). Each skull was tattooed with an individual number for distinction purposes, as approved by the ethics committee of the Centre du Don des Corps (Université Paris Descartes, Paris, France). Before being CT-scanned, each skull was degassed in water for at least 48 hours at 20 mbar to remove trapped air bubbles in the skull using a vacuum pump (diaphragm pump N810.3FT.18, KNF Neuberger, Freiburg, Germany). CT-scans were then acquired with a medical scanner (Revolution EVO, GE Medical Systems, Chicago, USA) at GHU Paris Psychiatrie & Neurosciences, France, with a slice thickness of 1.25 mm, an in-plane resolution of 0.625 mm and an interslice spacing of 1.25 mm.

For acoustic parameter estimation, each CT-scan was thresholded between $\text{HU}_{\min} = 0$ and $\text{HU}_{\max} = 2400$. The conversion from HU-maps to acoustic maps was done according to the linear model described by Marsac et al. [39]:

$$c(x,y,z) = c_{\text{water}} + (c_{\text{bone}} - c_{\text{water}})\frac{\text{HU}(x,y,z) - \text{HU}_{\min}}{\text{HU}_{\max} - \text{HU}_{\min}},$$

$$\rho(x,y,z) = \rho_{\text{water}} + (\rho_{\text{bone}} - \rho_{\text{water}})\frac{\text{HU}(x,y,z) - \text{HU}_{\min}}{\text{HU}_{\max} - \text{HU}_{\min}},$$

where $c_{\text{water}} = 1485$ m/s, $c_{\text{bone}} = 3100$ m/s, and $\rho_{\text{bone}} = 1900$ kg/m^3 [40].

The attenuation was neglected in this numerical model, as was done in previous work on transcranial phase estimation [41,42].

The skull acoustic maps were interpolated to an isotropic spatial resolution of 6 points per wavelength in water at 1 MHz, corresponding to $\Delta x = \Delta y = \Delta z = 248\ \mu$m.

C. Transcranial acoustic lens design

The skull acoustic maps were imported in numerical simulations performed on MATLAB with the k-Wave toolbox, by solving the set of equations described in II. A with a Courant-Friedrichs-Lewy number equal to 0.3 in cortical bone.

The profiles of two sets of transcranial lenses are computed using the same method as the one described in II. A. for homogeneous simulations, except that the source is placed at the geometric focus of the transducer, and the skull acoustic maps distort the recorded phase maps. Transcranial lenses are designed with a design frequency

$\nu_D = 683$ kHz, corresponding to one of the resonant frequencies of the transducer used in experiments.

A mould was then 3D-printed (Prusa i3 MK3, Prusa Research, Prague, Czech Republic) with a vertical precision of $200\ \mu$m to cast the acoustic lens. The material used to cast the lens is a silicone (Elite Double 8, Zhermack SpA, Badia Polesine, Italy) with the following acoustic properties: $c_{\text{lens}} = 1000$ m/s, $\rho_{\text{lens}} = 1040$ kg/m^3 [43]. The catalyst and the base were mixed together (1:1 ratio) and was then poured into the cast.

D. Intensity maps measurements and post-processing

A custom single-element transducer with a 100 mm radius of curvature and 100 mm aperture (Imasonic, Voray-sur-l'Ognon, France) was used in the experiments. It was driven at 500 kHz, 683 kHz and 1000 kHz, which are three of the resonance frequencies of the transducer. The input signal of the transducer was generated by an arbitrary waveform generator (33220A, Agilent Technologies, Santa Clara, CA, USA), and was then amplified (75A250, Amplifier Research, Souderton, PA, USA). The pressure field measurement was performed with a needle hydrophone (HNC-0400, Onda Corporation, Sunnyvale, CA, USA) equipped with a pre-amplifier (AH-2020-025, Onda Corporation, Sunnyvale, CA, USA) and an amplifier (AH-2020-DCBSW, Onda Corporation, Sunnyvale, CA, USA). The electrical signal acquired by this measurement line was digitised by a digital acquisition card (HS5, TiePie, Sneek, Netherlands). The hydrophone was mounted on a 3-axis motor assembly (ESP-301, Newport, Irvine, CA, USA). Prior to the ultrasound experiments, skulls were degassed.

For each of the driving frequency of the transducer four sets of experiments were performed. First, the acoustic focus location was determined by iteratively scanning around the geometric focus of the transducer, with no skull or lens interposed. The pressure signal was then recorded in a $16\lambda \times 16\lambda$ grid belonging to the focal plane and averaged 10 times with no skull. The amplitude and phase of the pressure wave were computed using the Fourier transform of the time series. The skull was then interposed between the transducer and its focal point with no lens to correct for aberrations. A 3D printed skull holder was designed for each skull to control the position of the skull relative to the transducer. The raw pressure signal was recorded in the focal plane of the transducer and averaged 10 times. The amplitude and phase of the pressure wave were obtained by computing the Fourier transform of the time series. Finally, for each of the crafted lens, the wrapped and the unwrapped one, the same measurement was done with the appropriate lens between the transducer and the skull to correct for its aberrations.

From the amplitude and phase of the pressure wave in the focal plane, the pressure amplitude was reconstructed in a 3D volume centred on the acoustic focus of the transducer using the angular spectrum method [44] and interpolated for visualisation and volumetric metrics computation purposes.

E. Targeting accuracy metrics

Three different metrics were defined to quantitatively evaluate the accuracy of the aberration corrections:

- The maximum intensity behind the skull, obtained from 3D reconstructions.
- The -6 dB volume of the focal spot behind the skull obtained from 3D reconstructions, which was compared to the volume of the focal spot in water, in the absence of skull.
- The normalised overlapping -6 dB volume, which corresponds to the intersection between the -6 dB volume in water, with no skull and the -6 dB volume behind the skull, either with or without aberration correction. The intersection of these two volumes is normalised by the volume of the focal spot behind the skull. This metric encompasses the size and shape of the focal spot as well as its position with regards to the target, which makes it a good metric to characterise the concentration of the acoustic intensity in the vicinity of the target.

III. RESULTS

A. Numerical simulations in a homogeneous medium

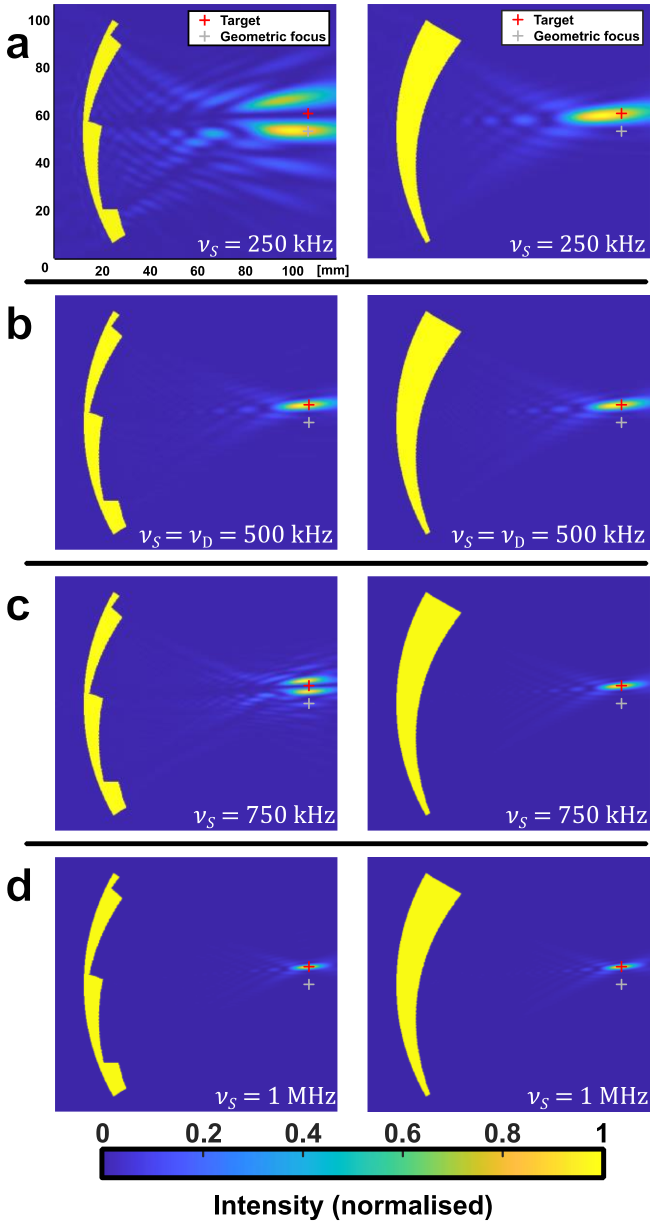

Fig. 1 – Computed normalised intensity with a wrapped lens (left panel) and an unwrapped lens (right panel) designed at 500 kHz. (a) – with a transducer driven at 250 kHz. (b) – with a transducer driven at 500 kHz. (c) – with a transducer driven at 750 kHz. (d) – with a transducer driven at 1 MHz.

Fig. 1 highlights the necessity of phase unwrapping to allow a unique acoustic lens to refocus at multiple frequencies. It can be noticed that the wrapped lens presents abrupt changes in thickness, which are due to the originally computed phase being constrained in the interval $[-\pi, \pi]$. To illustrate why phase wrapped lenses do not work at all frequencies, one can consider a simplistic example which consists in a lens designed at ν_D and composed of two parts with a constant thickness (e_1 and e_2 respectively) such that the abrupt thickness change between the two parts corresponds to a 2π difference at ν_D. When a wave front propagates through this lens at a frequency $\nu_S \neq \nu_D$, the phase difference between the portions of the wave front going through each part of the lens is, as per Eq. (II. 1):

$$\phi_{2,\nu_S} - \phi_{1,\nu_S} = 2\pi \frac{\nu_S}{\nu_D}.$$

These e_1 and e_2 thicknesses can be considered as the lens thicknesses right before and right after each thickness jump in Fig. 1 left panel. If ν_S is an integer multiple of ν_D as is the case in Fig. 1b left and Fig. 1d left, both portions of the wave front will interfere constructively. In an extreme case scenario where $\nu_S = 1.5\,\nu_D$ the wave fronts will interfere destructively and thus prevents an efficient focusing of the wave (Fig. 1c left).

On the other hand, the unwrapped lens focuses the wave effectively at any of the tested frequencies. This is due to the fact that the phase unwrapping process allows to transform the original phase map, constrained to $[-\pi, \pi]$, to an unwrapped phase map that is not bound to this interval. As such, the unwrapped phase map $\Phi(M)$ can be linearly related to the time-of-flight of the signal $\Delta t(M)$: $\Phi(M) = 2\pi\nu_D \Delta t(M)$, which substituted into Eq. (II. 1) allows the frequency dependent terms to cancel out, hence yielding:

$$e(M) = \frac{\Delta t(M)}{\frac{1}{c_{\text{water}}} - \frac{1}{c_{\text{lens}}}} + K, \qquad (\text{III}.2)$$

which is independent of the frequency, provided that the medium is non-dispersive (i.e. $\Delta t(M)$ does not depend on the frequency). It was reported that the skull was weakly dispersive between 0.3 MHz and 2 MHz [4,45], supporting the hypothesis that phase unwrapped lenses could be able to correct for skull aberrations within the same range of frequency.

B. Transcranial experimental validation at the design frequency of the lens

The intensity maps measured at the design frequency of the lenses are shown on Fig. 2 for skull A. The results for the other skulls are available in the Supplemental Material [46].

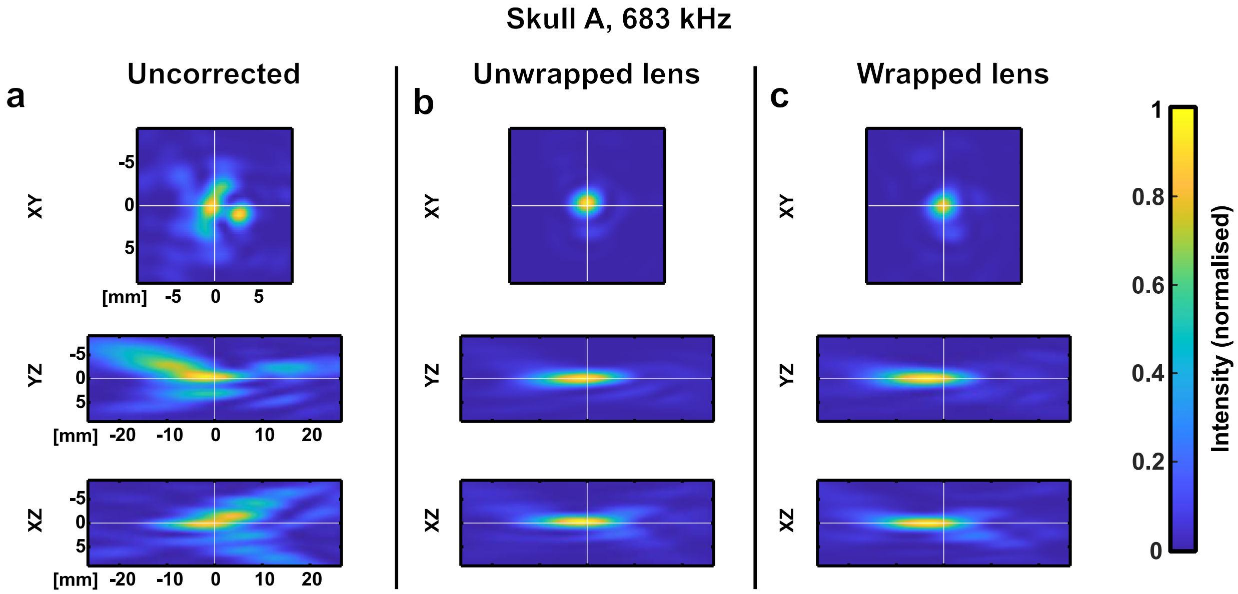

Fig. 2 – Measured intensity at 683 kHz for each condition on skull A. The white cross are centred on the location of the acoustic focus in water. (a): measured intensity with no lens. (b): measured intensity with a phase unwrapped lens. (c): measured intensity with a phase wrapped lens.

Uncorrected scans (Fig. 2a) exhibit a degraded focusing due to the presence of the skull. Two main spots are visible on Fig. 2a in the focal plane of the transducer.

Wrapped (Fig. 2c) and unwrapped lenses (Fig. 2b) allow to correct for skull aberrations at the design frequency of the lens. Higher secondary lobes can be seen on the measurement made with the wrapped lens. The irregularities induced by the phase jumps are not supposed to disrupt the coherence of the wave as they correspond to a 2π phase difference. Nevertheless, it can be hypothesized that the irregularities induce refraction. Such refraction was not taken into account in the design of the lens. Iterative simulation-based optimization could help mitigate this effect. This is beyond the current work and would require an extension of the work previously introduced in homogenous media [47] and would benefit from the reduction of the simulation time required for transcranial simulations [48].

C. Multifrequency transcranial focusing experiments

The intensity maps at 500 kHz obtained with lenses designed at 683 kHz are shown on Fig. 3. The results for the other skulls at 500 kHz are available in the Supplemental Material [46].

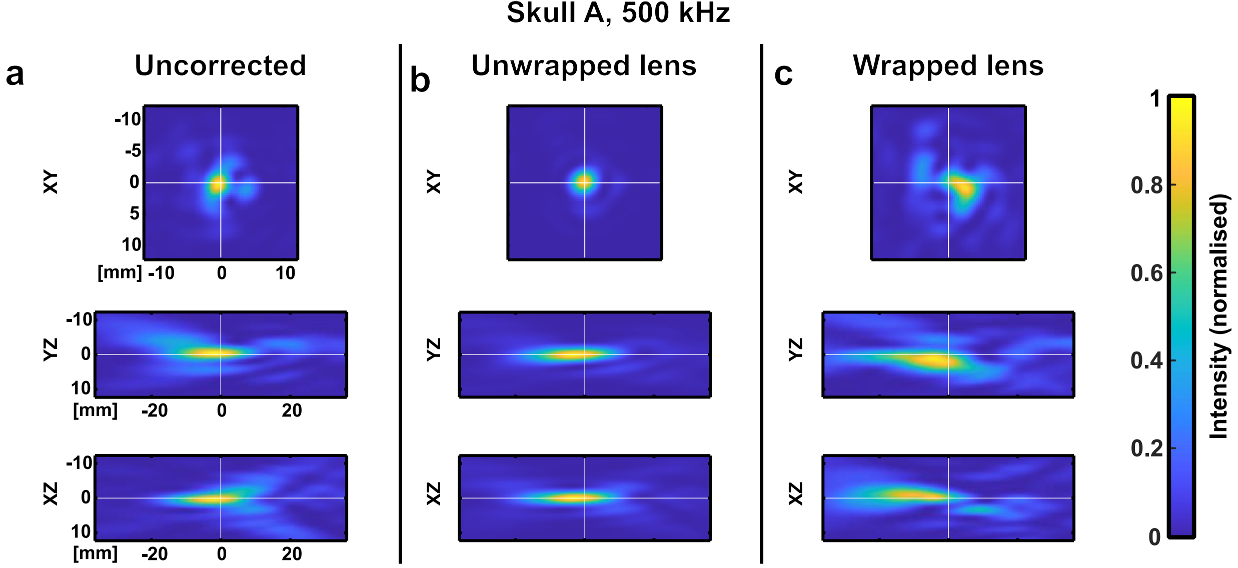

Fig. 3 – Measured intensity at 500 kHz for each condition on skull A. The white cross are centred on the location of the acoustic focus in water. (a): measured intensity with no lens. (b): measured intensity with a phase unwrapped lens. (c): measured intensity with a phase wrapped lens.

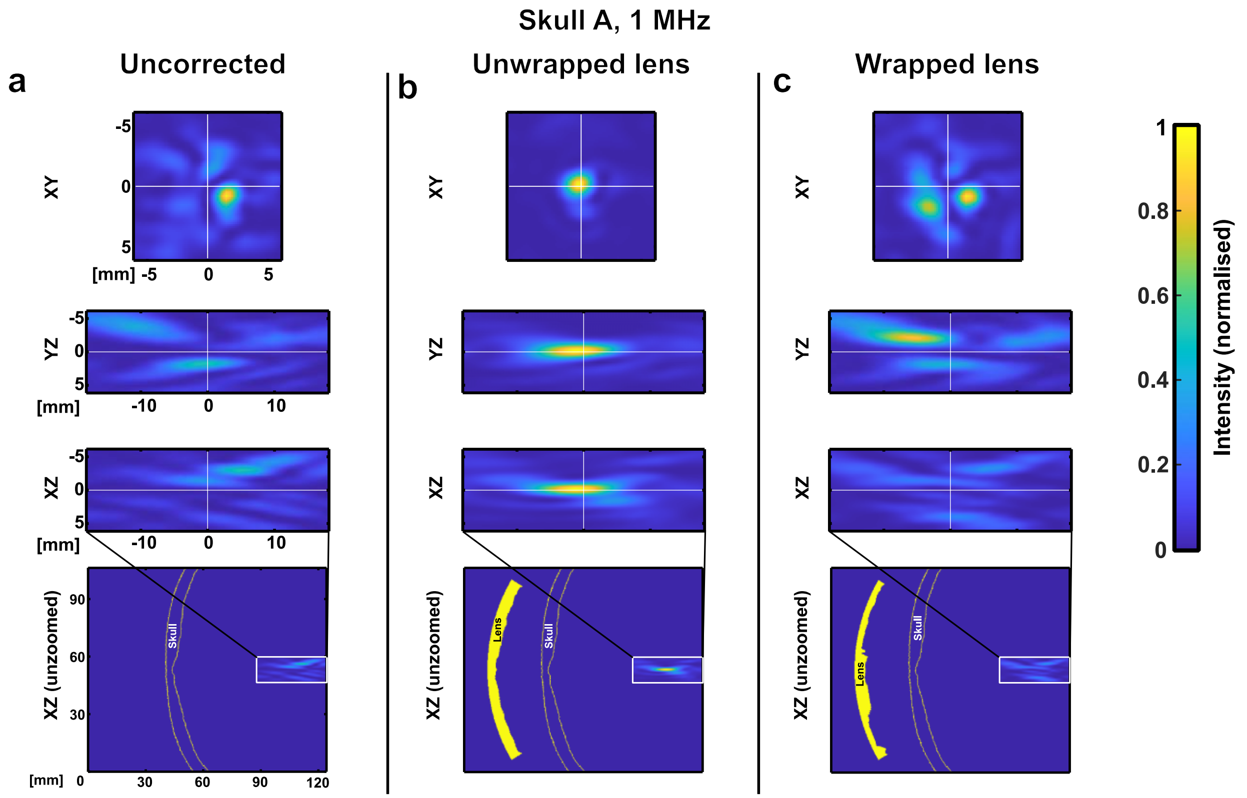

Fig. 4 – Measured intensity at 1 MHz for each condition on skull A. The white cross are centred on the location of the acoustic focus in water. (a): measured intensity with no lens. (b): measured intensity with a phase unwrapped lens. (c): measured intensity with a phase wrapped lens. For each condition, a large field of view version of the intensity map in the XZ plane is provided to visualize the skull and lenses geometry.

The uncorrected intensity map at 500 kHz (Fig. 3a) is less distorted than the one obtained at 683 kHz (Fig. 2a) and looks better than the wrapped lens focusing (Fig. 3c), the latter being strongly affected by the frequency change, as explained in section III. A. The unwrapped lens however still allows to correct for the skull aberrations at this frequency (Fig. 3b).

The intensity maps obtained at 1 MHz with the same lenses are shown on Fig. 4. The results for the other skulls at 1 MHz are available in the Supplemental Material [46].

The uncorrected intensity map (Fig. 4a) is highly distorted by the presence of the skull at 1 MHz, highlighting the need for aberration correction at high frequency. The wrapped lens designed at 683 kHz (Fig. 4c) is not capable of correcting for such aberrations at 1 MHz for the same reason as previously mentioned. The unwrapped lens (Fig. 4b) still exhibits a tight focusing at this frequency, thus achieving broadband aberration correction.

The broadband correction highlighted by Fig. 3 and Fig. 4 for the unwrapped lens suggests that dispersion is negligible in skull and silicone for this frequency range.

The inability of wrapped lenses to compensate for skull aberrations at frequencies different than their design frequency can also be explained in the light of the Rayleigh criterion which states that an optical instrument would offer performance close to that of an ideal system as long as the optical path difference remains below one-quarter of a wavelength [49]. In our case the phase difference induced by the lens should remain below $\pi/2$. As discussed previously a 2π phase jump obtained at ν_D induces a phase shift of $2\pi\frac{\nu_S}{\nu_D}$ when a wave propagates through the lens at ν_S. The phase difference can be expressed as:

$$\Delta\phi_{\nu_D,\nu_S} = 2\pi\left|\frac{\nu_S}{\nu_D}-1\right|.$$

Using a design frequency of $\nu_D = 683$ kHz, this corresponds to $\Delta\phi_{\nu_D,\nu_S} = 1.68$ rad and $\Delta\phi_{\nu_D,\nu_S} = 2.92$ rad at $\nu_S = 500$ kHz and $\nu_S = 1$ MHz respectively. Neither of these values fit the Rayleigh criterion, which might explain the important defocusing of the wave when the design frequency of the wrapped lens differs from the driving frequency of the transducer.

D. Targeting accuracy metrics

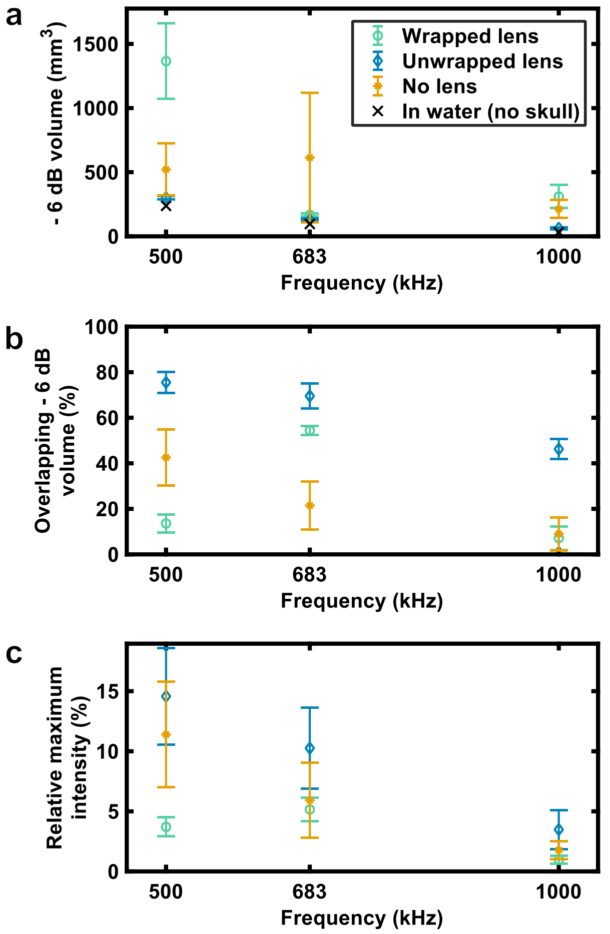

Fig. 5 – Mean and standard deviation of the metrics obtained from the measurements made on three skulls. (a) – -6 dB volume in mm^3 computed from the 3D field reconstructions. (b) – Normalised overlapping -6 dB volume computed from the 3D field reconstructions. (c) – Maximum intensity in the reconstructed volume normalised by the maximum intensity in water. For (b)-(c), the result in water with no skull is not shown since it is equal to 100% by definition of the metrics.

Fig. 5 represents the means and standard deviations of the metrics on three different skulls, for the three frequencies. The detailed results for each skull are available in Table S.I in the Supplemental Material [46]. The -6 dB volume (Fig. 5a) shows that both the wrapped lenses and unwrapped lenses work at the design frequency of the lens, since the sizes of the focal spots behind the skull are similar to the size of the reference focal spot. This is true for each of the three skulls tested, as assessed by the low standard deviations for both lenses. As could be already seen qualitatively from the intensity maps in Section III. B. and III. C., Fig. 5a confirms that the unwrapped lenses are able to restore a tight focusing at each of the three frequencies.

The intensity maps displayed in III. C. might suggest that correcting for skull aberrations is not always necessary at low frequencies. Nonetheless, Fig. 5a disproves this hypothesis by highlighting a higher standard deviation across the uncorrected cases. At 500 kHz, the standard deviation corresponds to 105% and 7% of the reference value without correction and with the unwrapped lens respectively (see Table S.I in the Supplemental Material [46]).

The overlapping -6 dB volume plot (Fig. 5b) and the maximum intensity measured behind the skull (Fig. 5c) confirm the broadband aspect of the aberrations correction of the unwrapped acoustic lens.

The wrapped lens underperforms the maximum intensity, even at its design frequency (Fig. 5c), with an average 49% relative drop compared to the unwrapped lens (see Table S.I in the Supplemental Material [46]). This demonstrates that even when focusing the wave at a single frequency, unwrapping the phase can significantly improve the intensity at focus. We attribute this phenomenon to refraction at the thickness jump in the wrapped lenses.

The important standard deviations of the maximum intensity retrieved behind skulls shown on Fig. 5c even when correcting for aberrations with phase unwrapped lenses are hypothesized to be due to the fact that each skull is intrinsically more or less attenuating due to its thickness and internal geometry. In addition to that, a decrease of the maximum retrieved intensity as the frequency increases is in line with the increase of the attenuation of the skull bone with the frequency [4,50].

IV. DISCUSSION AND CONCLUSIONS

This work demonstrates the advantage of phase unwrapping for the design of multi-frequency acoustic lenses.

Phase unwrapping is shown to both improve the performance of single-frequency lenses as well as to enable multi-frequency lenses in homogenous lateral beam steering simulations and in transcranial focusing experiments. This is due to the fact that the phase received on the surface of a transducer is not always contained in a 2π interval after propagation of the wave from its initial target.

The presence of thickness jumps on the surface of the lens depends on many parameters, among which is the geometry of the transducer. If the transducer is not spherical as is the case in many transcranial lens studies [15,51,52], the phase shifts to focus the wave will inevitably span in an interval larger than 2π. In the case of a spherical transducer, the aperture plays a role in the presence of phase jumps, since a larger transducer aperture will include a larger section of the skull and a larger span of the phase required to refocus the wave [33,39,41,53–57]. The geometry of the section of the skull through which the wave propagates will also play a role, since a skull section of quasi-uniform thickness will require little correction as opposed to a more undulating skull [58]. For simple cases, e.g. considering a small aperture spherical transducer focusing through a slightly aberrating medium at a low frequency, the phase maps might be entirely contained in a 2π interval. In such cases, limiting the amount of residual phase jumps may be done by simply adjusting the phase reference.

According to Eq. (III. 2), unwrapped phase masks can be obtained from time-of-flights. As such, it could be envisioned to use ray-tracing simulations to obtain the phase masks in a more computationally efficient way [41,59].

A limitation of phase unwrapped lenses is that provided that the unwrapped phase span in an interval larger than 2π, the resulting lens will be thicker than the one that could be obtained by wrapping the phase, according to Eq. (II. 1).

Due to their broadband properties, unwrapped acoustic lenses could be used to adjust the frequency with a fixed setup for transcranial biomedical applications such as deep brain ultrasound stimulation [32,60–63] or high intensity focused ultrasound therapies [64,65]. Broadband acoustic lenses could also help increase the data transfer rate of spatially selective airborne ultrasound transmission with a limited number of sources [66–68].

Since the skull bone has a high impedance compared to that of water, it could be envisioned to couple such acoustic lenses with metamaterials aimed at enhancing the transmission efficacy of ultrasound through biological layers [69].

ACKNOWLEDGMENTS

The authors thank Thomas Manuel for proofreading this article. This work was supported by the "Agence Nationale de la Recherche" under the program "Ultrastim" [ANR-20-CE19-0013].

BIBLIOGRAPHY

[1] Y. Kim, *Advances in MR Image-Guided High-Intensity Focused Ultrasound Therapy*, International Journal of Hyperthermia **31**, 225 (2015).

[2] E. S. Ebbini and G. Ter Haar, *Ultrasound-Guided Therapeutic Focused Ultrasound: Current Status and Future Directions*, International Journal of Hyperthermia **31**, 77 (2015).

[3] D. Tyshlek, J.-F. Aubry, G. ter Haar, A. Hananel, J. Foley, M. Eames, N. Kassell, and H. H. Simonin, *Focused Ultrasound Development and Clinical Adoption: 2013 Update on the Growth of the Field*, J Ther Ultrasound **2**, 2 (2014).

[4] F. J. Fry and J. E. Barger, *Acoustical Properties of the Human Skull*, The Journal of the Acoustical Society of America **63**, 1576 (1978).

[5] A. Sanjeev, V. Trivedi, and Z. Zalevsky, *Optical Reciprocity Induced Wavefront Shaping for Axial and Lateral Shifting of Focus through a Scattering Medium*, Sci Rep **12**, 6387 (2022).

[6] S. M. Popoff, G. Lerosey, R. Carminati, M. Fink, A. C. Boccara, and S. Gigan, *Measuring the Transmission Matrix in Optics: An Approach to the Study and Control of Light Propagation in Disordered Media*, Phys. Rev. Lett. **104**, 100601 (2010).

[7] Z. Yaqoob, D. Psaltis, M. S. Feld, and C. Yang, *Optical Phase Conjugation for Turbidity Suppression in Biological Samples*, Nature Photon **2**, 110 (2008).

[8] X. Xu, H. Liu, and L. V. Wang, *Time-Reversed Ultrasonically Encoded Optical Focusing into Scattering Media*, Nature Photon **5**, 154 (2011).

[9] M. Lyu, H. Wang, G. Li, S. Zheng, and G. Situ, *Learning-Based Lensless Imaging through Optically Thick Scattering Media*, AP **1**, 036002 (2019).

[10] J.-F. Aubry, M. Tanter, M. Pernot, J.-L. Thomas, and M. Fink, *Experimental Demonstration of Noninvasive Transskull Adaptive Focusing Based on Prior Computed Tomography Scans*, The Journal of the Acoustical Society of America **113**, 84 (2003).

[11] G. T. Clement, J. Sun, T. Giesecke, and K. Hynynen, *A Hemisphere Array for Non-Invasive Ultrasound Brain Therapy and Surgery*, Phys. Med. Biol. **45**, 3707 (2000).

[12] M. Pernot, J.-F. Aubry, M. Tanter, J.-L. Thomas, and M. Fink, *High Power Transcranial Beam Steering for Ultrasonic Brain Therapy*, Phys. Med. Biol. **48**, 2577 (2003).

[13] J. Song and K. Hynynen, *Feasibility of Using Lateral Mode Coupling Method for a Large Scale Ultrasound Phased Array for Noninvasive Transcranial Therapy*, IEEE Trans. Biomed. Eng. **57**, 124 (2010).

[14] R. Lalonde and J. W. Hunt, *Variable Frequency Field Conjugate Lenses for Ultrasound Hyperthermia*, IEEE Trans. Ultrason., Ferroelect., Freq. Contr. **42**, 825 (1995).

[15] Z. Hu, Y. Yang, L. Xu, Y. Hao, and H. Chen, *Binary Acoustic Metasurfaces for Dynamic Focusing of Transcranial Ultrasound*, Front. Neurosci. **16**, 984953 (2022).

[16] M. D. Brown, B. T. Cox, and B. E. Treeby, *Design of Multi-Frequency Acoustic Kinoforms*, Appl. Phys. Lett. **111**, 244101 (2017).

[17] R. E. Beard, R. L. Magin, L. A. Frizzell, and C. A. Cain, *An Annular Focus Ultrasonic Lens for Local Hyperthermia Treatment of Small Tumors*, Ultrasound in Medicine & Biology **8**, 177 (1982).

[18] R. J. Lalonde, A. Worthington, and J. W. Hunt, *Field Conjugate Acoustic Lenses for Ultrasound Hyperthermia*, IEEE Transactions on Ultrasonics, Ferroelectrics, and Frequency Control **40**, 592 (1993).

[19] X. Wu and M. Sherar, *Theoretical Evaluation of Moderately Focused Spherical Transducers and Multi-Focus Acoustic Lens/Transducer Systems for Ultrasound Thermal Therapy*, Phys. Med. Biol. **47**, 1603 (2002).

[20] G. Maimbourg, A. Houdouin, T. Deffieux, M. Tanter, and J.-F. Aubry, *Steering Capabilities of an Acoustic Lens for Transcranial Therapy: Numerical and Experimental Studies*, IEEE Transactions on Biomedical Engineering **67**, 27 (2020).

[21] S. Jiménez-Gambín, N. Jiménez, J. M. Benlloch, and F. Camarena, *Holograms to Focus Arbitrary Ultrasonic Fields through the Skull*, Phys. Rev. Applied **12**, 014016 (2019).

[22] S. Jiménez-Gambín, N. Jiménez, and F. Camarena, *Transcranial Focusing of Ultrasonic Vortices by Acoustic Holograms*, Phys. Rev. Applied **14**, 054070 (2020).

[23] M. D. Brown, *Phase and Amplitude Modulation with Acoustic Holograms*, Appl. Phys. Lett. **115**, 053701 (2019).

[24] M. D. Brown, B. T. Cox, and B. E. Treeby, *Stackable Acoustic Holograms*, Appl. Phys. Lett. **116**, 261901 (2020).

[25] K. Melde, A. G. Mark, T. Qiu, and P. Fischer, *Holograms for Acoustics*, Nature **537**, 518 (2016).

[26] T. Fjield, C. E. Silcox, and K. Hynynen, *Low-Profile Lenses for Ultrasound Surgery*, 12 (1999).

[27] H. Zhou, L. Chen, F. Shen, K. Guo, and Z. Guo, *Broadband Achromatic Metalens in the Midinfrared Range*, Phys. Rev. Appl. **11**, 024066 (2019).

[28] P. Wang, N. Mohammad, and R. Menon, *Chromatic-Aberration-Corrected Diffractive Lenses for Ultra-Broadband Focusing*, Sci Rep **6**, 1 (2016).

[29] E. J. Fernández, A. Unterhuber, B. Považay, B. Hermann, P. Artal, and W. Drexler, *Chromatic Aberration Correction of the Human Eye for Retinal Imaging in the near Infrared*, Opt. Express, OE **14**, 6213 (2006).

[30] C. Constans, T. Deffieux, P. Pouget, M. Tanter, and J.-F. Aubry, *A 200–1380-kHz Quadrifrequency Focused Ultrasound Transducer for Neurostimulation in Rodents and Primates: Transcranial* In Vitro *Calibration and Numerical Study of the Influence of Skull Cavity*, IEEE Trans. Ultrason., Ferroelect., Freq. Contr. **64**, 717 (2017).

[31] M. Plaksin, S. Shoham, and E. Kimmel, *Intramembrane Cavitation as a Predictive Bio-Piezoelectric Mechanism for Ultrasonic Brain Stimulation*, Phys. Rev. X **4**, 011004 (2014).

[32] R. L. King, J. R. Brown, W. T. Newsome, and K. B. Pauly, *Effective Parameters for Ultrasound-Induced In Vivo Neurostimulation*, Ultrasound in Medicine & Biology **39**, 312 (2013).

[33] N. Lu, T. L. Hall, J. R. Sukovich, S. W. Choi, J. Snell, N. McDannold, and Z. Xu, *Two-Step Aberration Correction: Application to Transcranial Histotripsy*, Phys. Med. Biol. **67**, 125009 (2022).

[34] B. E. Treeby and B. T. Cox, *K-Wave: MATLAB Toolbox for the Simulation and Reconstruction of Photoacoustic Wave Fields*, JBO **15**, 021314 (2010).

[35] B. E. Treeby, J. Jaros, A. P. Rendell, and B. T. Cox, *Modeling Nonlinear Ultrasound Propagation in Heterogeneous Media with Power Law Absorption Using a K-Space Pseudospectral Method*, The Journal of the Acoustical Society of America **131**, 4324 (2012).

[36] D. Zheng and F. Da, *A Novel Algorithm for Branch Cut Phase Unwrapping*, Optics and Lasers in Engineering **49**, 609 (2011).

[37] M. Costantini, *A Novel Phase Unwrapping Method Based on Network Programming*, IEEE Transactions on Geoscience and Remote Sensing **36**, 813 (1998).

[38] Z. Zhao, H. Zhang, Z. Xiao, H. Du, Y. Zhuang, C. Fan, and H. Zhao, *Robust 2D Phase Unwrapping Algorithm Based on the Transport of Intensity Equation*, Meas. Sci. Technol. **30**, 015201 (2019).

[39] L. Marsac, D. Chauvet, R. La Greca, A.-L. Boch, K. Chaumoitre, M. Tanter, and J.-F. Aubry, Ex Vivo *Optimisation of a Heterogeneous Speed of Sound Model of the Human Skull for Non-Invasive Transcranial Focused Ultrasound at 1 MHz*, International Journal of Hyperthermia **33**, 635 (2017).

[40] F. A. Duck, *Physical Properties of Tissue: A Comprehensive Reference Book* (Academic Press, London, 1990).

[41] T. Bancel, A. Houdouin, P. Annic, I. Rachmilevitch, Y. Shapira, M. Tanter, and J.-F. Aubry, *Comparison Between Ray-Tracing and Full-Wave Simulation for Transcranial Ultrasound Focusing on a Clinical System Using the Transfer Matrix Formalism*, IEEE Trans. Ultrason., Ferroelect., Freq. Contr. **68**, 2554 (2021).

[42] N. McDannold, P. J. White, and R. Cosgrove, *Elementwise Approach for Simulating Transcranial MRI-Guided Focused Ultrasound Thermal Ablation*, Phys. Rev. Res. **1**, 033205 (2019).

[43] G. Maimbourg, A. Houdouin, T. Deffieux, M. Tanter, and J.-F. Aubry, *3D-Printed Adaptive Acoustic Lens as a Disruptive Technology for Transcranial Ultrasound Therapy Using Single-Element Transducers*, Phys. Med. Biol. **63**, 025026 (2018).

[44] X. Zeng and R. J. McGough, *Evaluation of the Angular Spectrum Approach for Simulations of Near-Field Pressures*, The Journal of the Acoustical Society of America **123**, 68 (2008).

[45] S. Pichardo, V. W. Sin, and K. Hynynen, *Multi-Frequency Characterization of the Speed of Sound and Attenuation Coefficient for Longitudinal Transmission of Freshly Excised Human Skulls*, Phys. Med. Biol. **56**, 219 (2010).

[46] See Supplemental Material at [URL Will Be Inserted by Publisher] for intensity maps obtained on two other skulls at the three tested frequencies; quantitative results for each tested skull.

[47] M. D. Brown, B. T. Cox, and B. E. Treeby, *Binary Volume Acoustic Holograms*, Phys. Rev. Appl. **19**, 044032 (2023).

[48] G. Maimbourg, J. Guilbert, T. Bancel, A. Houdouin, G. Raybaud, M. Tanter, and J.-F. Aubry, *Computationally Efficient Transcranial Ultrasonic Focusing: Taking Advantage of the High Correlation Length of the Human Skull*, IEEE Transactions on Ultrasonics, Ferroelectrics, and Frequency Control **67**, 1993 (2020).

[49] A. E. Conrady and R. Kingslake, *Applied Optics and Optical Design* (Courier Corporation, 1992).

[50] H. Estrada, J. Rebling, J. Turner, and D. Razansky, *Broadband Acoustic Properties of a Murine Skull*, Phys. Med. Biol. **61**, 1932 (2016).

[51] G. Kook, Y. Jo, C. Oh, X. Liang, J. Kim, S.-M. Lee, S. Kim, J.-W. Choi, and H. J. Lee, *Multifocal Skull-Compensated Transcranial Focused Ultrasound System for Neuromodulation Applications Based on Acoustic Holography*, Microsyst Nanoeng **9**, 1 (2023).

[52] D. Andrés, N. Jiménez, J. M. Benlloch, and F. Camarena, *Numerical Study of Acoustic Holograms for Deep-Brain Targeting through the Temporal Bone Window*, Ultrasound in Medicine & Biology **48**, 872 (2022).

[52] M. Wintermark, N. J. Tustison, W. J. Elias, J. T. Patrie, W. Xin, N. Demartini, M. Eames, S. Sumer, B. Lau, A. Cupino et al., *T1-Weighted MRI as a Substitute to CT for Refocusing Planning in MR-Guided Focused Ultrasound*, Phys. Med. Biol. **59**, 3599 (2014).

[54] G. W. Miller, M. Eames, J. Snell, and J.-F. Aubry, *Ultrashort Echo-Time MRI versus CT for Skull Aberration Correction in MR-Guided Transcranial Focused Ultrasound:* In Vitro *Comparison on Human Calvaria: UTE-Based Skull Aberration Correction for MR-Guided HIFU*, Med. Phys. **42**, 2223 (2015).

[55] G. F. Pinton, J.-F. Aubry, and M. Tanter, *Direct Phase Projection and Transcranial Focusing of Ultrasound for Brain Therapy*, IEEE Transactions on Ultrasonics, Ferroelectrics, and Frequency Control **59**, 1149 (2012).

[56] F. Marquet, M. Pernot, J.-F. Aubry, G. Montaldo, L. Marsac, M. Tanter, and M. Fink, *Non-Invasive Transcranial Ultrasound Therapy Based on a 3D CT Scan: Protocol Validation and* in Vitro *Results*, Phys. Med. Biol. **54**, 2597 (2009).

[57] E. A. Kaye, Y. Hertzberg, M. Marx, B. Werner, G. Navon, M. Levoy, and K. B. Pauly, *Application of Zernike Polynomials towards Accelerated Adaptive Focusing of Transcranial High Intensity Focused Ultrasound*, Medical Physics **39**, 6254 (2012).

[57] D. Attali, T. Tiennot, M. Schafer, E. Fouragnan, J. Sallet, C. F. Caskey, R. Chen, G. Darmani, E. J. Bubrick, C. Butler et al., *Three-Layer Model with Absorption for Conservative Estimation of the Maximum Acoustic Transmission Coefficient through the Human Skull for Transcranial Ultrasound Stimulation*, Brain Stimulation (2022).

[59] T. Wang and Y. Jing, *Transcranial Ultrasound Imaging with Speed of Sound-Based Phase Correction: A Numerical Study*, Phys. Med. Biol. **58**, 6663 (2013).

[60] Y. Tufail, A. Matyushov, N. Baldwin, M. L. Tauchmann, J. Georges, A. Yoshihiro, S. I. H. Tillery, and W. J. Tyler, *Transcranial Pulsed Ultrasound Stimulates Intact Brain Circuits*, Neuron **66**, 681 (2010).

[61] S.-S. Yoo, A. Bystritsky, J.-H. Lee, Y. Zhang, K. Fischer, B.-K. Min, N. J. McDannold, A. Pascual-Leone, and F. A. Jolesz, *Focused Ultrasound Modulates Region-Specific Brain Activity*, NeuroImage **56**, 1267 (2011).

[62] T. Deffieux, Y. Younan, N. Wattiez, M. Tanter, P. Pouget, and J.-F. Aubry, *Low-Intensity Focused Ultrasound Modulates Monkey Visuomotor Behavior*, Current Biology **23**, 2430 (2013).

[63] P.-F. Yang, M. A. Phipps, A. T. Newton, S. Jonathan, T. J. Manuel, J. C. Gore, W. A. Grissom, C. F. Caskey, and L. M. Chen, *Differential Dose Responses of Transcranial Focused Ultrasound at Brain Regions Indicate Causal Interactions*, Brain Stimulation **15**, 1552 (2022).

[63] W. J. Elias, N. Lipsman, W. G. Ondo, P. Ghanouni, Y. G. Kim, W. Lee, M. Schwartz, K. Hynynen, A. M. Lozano, B. B. Shah et al., *A Randomized Trial of Focused Ultrasound Thalamotomy for Essential Tremor*, New England Journal of Medicine **375**, 730 (2016).

[64] R. Martínez-Fernández, J. U. Máñez-Miró, R. Rodríguez-Rojas, M. del Álamo, B. B. Shah, F. Hernández-Fernández, J. A. Pineda-Pardo, M. H.G. Monje, B. Fernández-Rodríguez, S. A. Sperling et al., *Randomized Trial of Focused Ultrasound Subthalamotomy for Parkinson's Disease*, New England Journal of Medicine **383**, 2501 (2020).

[66] A. Derode, A. Tourin, J. de Rosny, M. Tanter, S. Yon, and M. Fink, *Taking Advantage of Multiple Scattering to Communicate with Time-Reversal Antennas*, Phys. Rev. Lett. **90**, 014301 (2003).

[67] W. Jiang and W. M. D. Wright, *Multichannel Ultrasonic Data Communications in Air Using Range-Dependent Modulation Schemes*, IEEE Trans. Ultrason., Ferroelect., Freq. Contr. **63**, 147 (2016).

[68] S. Holm, O. B. Hovind, S. Rostad, and R. Holm, *Indoors Data Communications Using Airborne Ultrasound*, in *Proceedings. (ICASSP '05). IEEE International Conference on Acoustics, Speech, and Signal Processing, 2005.*, Vol. 3 (IEEE, Philadelphia, Pennsylvania, USA, 2005), pp. 957–960.

[69] J. Wang, F. Allein, N. Boechler, J. Friend, and O. Vazquez-Mena, *Design and Fabrication of Negative-Refractive-Index Metamaterial Unit Cells for Near-Megahertz Enhanced Acoustic Transmission in Biomedical Ultrasound Applications*, Phys. Rev. Appl. **15**, 024025 (2021).